

Molecular tuning boosts asymmetric C-C coupling for CO conversion to acetate

Received: 27 July 2023

Accepted: 15 April 2024

Published online: 29 April 2024



Jie Ding^{1,9}, Fuhua Li^{1,9}, Xinyi Ren², Yuhang Liu³, Yifan Li⁴, Zheng Shen², Tian Wang⁵, Weijue Wang², Yang-Gang Wang⁶, Yi Cui⁴, Hongbin Yang³✉, Tianyu Zhang⁷✉ & Bin Liu^{1,8}✉

Electrochemical carbon dioxide/carbon monoxide reduction reaction offers a promising route to synthesize fuels and value-added chemicals, unfortunately their activities and selectivities remain unsatisfactory. Here, we present a general surface molecular tuning strategy by modifying Cu₂O with a molecular pyridine-derivative. The surface modified Cu₂O nanocubes by 4-mercaptopyridine display a high Faradaic efficiency of greater than 60% in electrochemical carbon monoxide reduction reaction to acetate with a current density as large as 380 mA/cm² in a liquid electrolyte flow cell. In-situ attenuated total reflectance surface-enhanced infrared absorption spectroscopy reveals stronger *CO signal with bridge configuration and stronger *OCCHO signal over modified Cu₂O nanocubes by 4-mercaptopyridine than unmodified Cu₂O nanocubes during electrochemical CO reduction. Density function theory calculations disclose that local molecular tuning can effectively regulate the electronic structure of copper catalyst, enhancing *CO and *CHO intermediates adsorption by the stabilization effect through hydrogen bonding, which can greatly promote asymmetric *CO-*CHO coupling in electrochemical carbon monoxide reduction reaction.

Acetate is an important chemical to manufacture food additives, solvents, medicine, etc^{1,2}. The global demand for acetate was 17.3 million tons in 2019 and is predicted to reach 24.5 million tons by 2025³. Nowadays, methanol carbonylation still serves as the main method to produce acetate, which is energy-consuming and environmentally unfriendly⁴⁻⁷. On the other hand, electrochemical carbon dioxide/carbon monoxide reduction reaction (CO₂RR/CORR) powered by renewable electricity provides a greener approach to make acetate⁸⁻¹². However, the selectivity and the partial current density towards the targeted acetate via CO₂RR/CORR are still

unsatisfactory, and the reaction pathway for CO₂RR/CORR to acetate remains ambiguous.

Cu-based electrocatalysts have been intensively studied in CO₂RR/CORR to make C₂₊ fuels/chemicals, but they still suffer from poor selectivity¹³. Various strategies have been applied to tackle the poor selectivity challenge, including alloying, facet engineering, surface regulation, etc¹⁴⁻²³. Among the different approaches, modifying Cu surface with certain small molecule was proposed as a promising route to modulate the reaction pathways for generation of C₂₊ fuels/chemicals^{24,25}.

¹Department of Materials Science and Engineering, City University of Hong Kong, Hong Kong SAR, China. ²CAS Key Laboratory of Science and Technology on Applied Catalysis, Dalian Institute of Chemical Physics, Chinese Academy of Sciences, Dalian, China. ³School of Materials Science and Engineering, Suzhou University of Science and Technology, Suzhou, China. ⁴Vacuum Interconnected Nanotech Workstation, Suzhou Institute of Nano-Tech and Nano-Bionics, Chinese Academy of Sciences, Suzhou, China. ⁵Department of Chemical & Biomolecular Engineering, National University of Singapore, Singapore, Singapore. ⁶Department of Chemistry and Guangdong Provincial Key Laboratory of Catalysis, Southern University of Science and Technology, Shenzhen, China. ⁷College of Environmental Science and Engineering, Beijing Forestry University, Beijing, China. ⁸Department of Chemistry & Center of Super-Diamond and Advanced Films (COSDAF), City University of Hong Kong, Hong Kong SAR, China. ⁹These authors contributed equally: Jie Ding, Fuhua Li. ✉e-mail: hbyang@dicp.ac.cn; tzhang@bjfu.edu.cn; bliu48@cityu.edu.hk

Molecules exhibited multiple-functions on CO₂RR determined by the structure of molecules^{26,27}. Molecular decoration is able to adjust the strength of intermediates adsorption and selectively stabilize certain intermediates through hydrogen bonding or enhance the adsorption of certain intermediates via confinement effect or regulating the catalyst's electronic structure to boost the catalytic performance^{28–30}. However, insufficient understanding of the underlying principle of small molecule modification on electrochemical CO₂RR/CORR remains a major factor hindering the development of this strategy.

In this work, we presented a universal strategy to modify Cu-based catalysts with 4-mercaptopyridine (pyS), including commercial Cu, Cu₂O, CuO as well as the as-prepared Cu₂O nanocubes, which could dramatically enhance the catalytic performance for electrochemical CORR to produce acetate. The molecular tuning induced by 4-mercaptopyridine over Cu surface enhanced the adsorption of reaction intermediates in CORR, improved the hydrogenation of *CO, facilitated asymmetric *CO-*CHO coupling and thus stimulated the CO-to-acetate conversion. The surface modified Cu₂O nanocubes by 4-mercaptopyridine (Cu₂O-pyS) exhibited a high acetate FE of >60% at a total current density of 380 mA cm⁻¹ in a liquid electrolyte flow cell, whose performance remained almost unchanged at 380 mA/cm² with an acetate FE over 60% for 100 h in a flow cell. The impressive CORR performance of Cu₂O-pyS originated from the boosted asymmetric C-C coupling induced by 4-mercaptopyridine modification, validated by in-situ ATR-SEIRAS measurements and DFT calculations.

Results

Catalyst preparation and CORR performance

Cu₂O nanocubes were synthesized and further functionalized with 4-mercaptopyridine. Cu₂O nanocubes with a mean size of ~50 nm were synthesized by a facile solution method and then modified with 4-mercaptopyridine under ultrasonication (Supplementary Fig. 1a). X-ray diffraction (XRD) of Cu₂O-pyS displays peaks at 29.6°, 36.4°, and 43.4°, which can be assigned to Cu₂O (110), Cu₂O (111) and Cu₂O (200),

respectively (JCPDS file NO. 05-0667, Supplementary Fig. 1b). Compared to unmodified Cu₂O nanocubes, the infrared spectrum of Cu₂O-pyS exhibits several characteristic peaks. The peaks at 788 cm⁻¹, 1460 cm⁻¹, and 1598 cm⁻¹ can be assigned to the stretching vibration of C=S, C=C and pyridine ring, respectively, demonstrating the successful introduction of 4-mercaptopyridine onto Cu₂O nanocubes (Supplementary Fig. 1c). Scanning electron microscopy (SEM) and transmission electron microscopy (TEM) images (Supplementary Figs. 2a, b and 3a, b) indicate that the Cu₂O-pyS maintains the well-defined nanocube morphology after 4-mercaptopyridine modification. High-resolution energy-dispersive X-ray spectroscopy (EDS) line scan and mapping over Cu₂O-pyS show homogeneous distribution of Cu, O, N, and S elements, suggesting successful attachment of 4-mercaptopyridine on the surface of Cu₂O nanocubes (Supplementary Figs. 2d and 3d). The clear lattice fringe of 0.213 nm observed on Cu₂O-pyS can be assigned to Cu₂O (200) (Supplementary Figs. 2c and 3e). The electronic structure of Cu₂O-pyS was probed by X-ray photoelectron spectroscopy (XPS) and it was found that the binding energy of Cu in Cu₂O-pyS was shifted towards higher binding energies after 4-mercaptopyridine modification (Supplementary Fig. 4a). High-resolution N 1s and S 2p XPS spectra of Cu₂O-pyS display clear peaks originating from 4-mercaptopyridine. The high-resolution N 1s XPS spectrum can be deconvoluted into pyridine N (397.5 eV) and N with different degrees of H acceptance, respectively³¹. The high-resolution S 2p XPS spectrum displays a peak at 162 eV (Supplementary Fig. 4b), indicating the formation of Cu-S bond³². The presence of thiolate and the absence of metal-N bond corroborate that 4-mercaptopyridine is linked on Cu₂O via the Cu-S bond.

The CORR was evaluated in a flow-cell electrolyzer to overcome the poor solubility of CO and the sluggish CO mass transport in aqueous solution (Supplementary Figs. 5 and 6)^{33–35}. The electrochemical performance of Cu₂O-pyS was also evaluated. As presented in Fig. 1a & Supplementary Fig. 7, CO could be electrochemically reduced on Cu₂O-pyS to acetate, exhibiting a total current density of 380 mA/cm² with an acetate FE (FE_{acetate}) as high as 62% at -0.85 V versus reversible

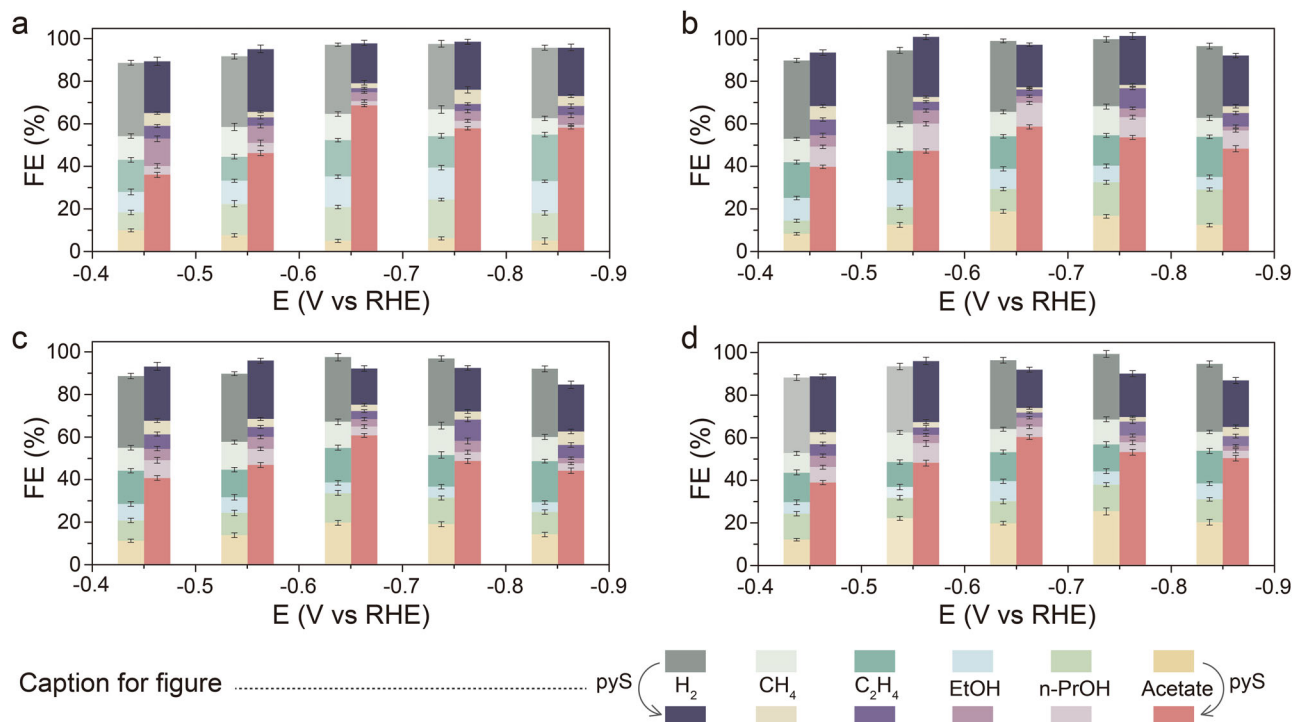


Fig. 1 | Electrochemical CORR performance. FE of various products for the as-prepared Cu₂O nanocubes and Cu₂O-pyS (a), commercial Cu and c-Cu-pyS (b), commercial Cu₂O and c-Cu₂O-pyS (c), and commercial CuO and c-CuO-pyS (d). Error bars represent the standard deviation of three replicate measurements.

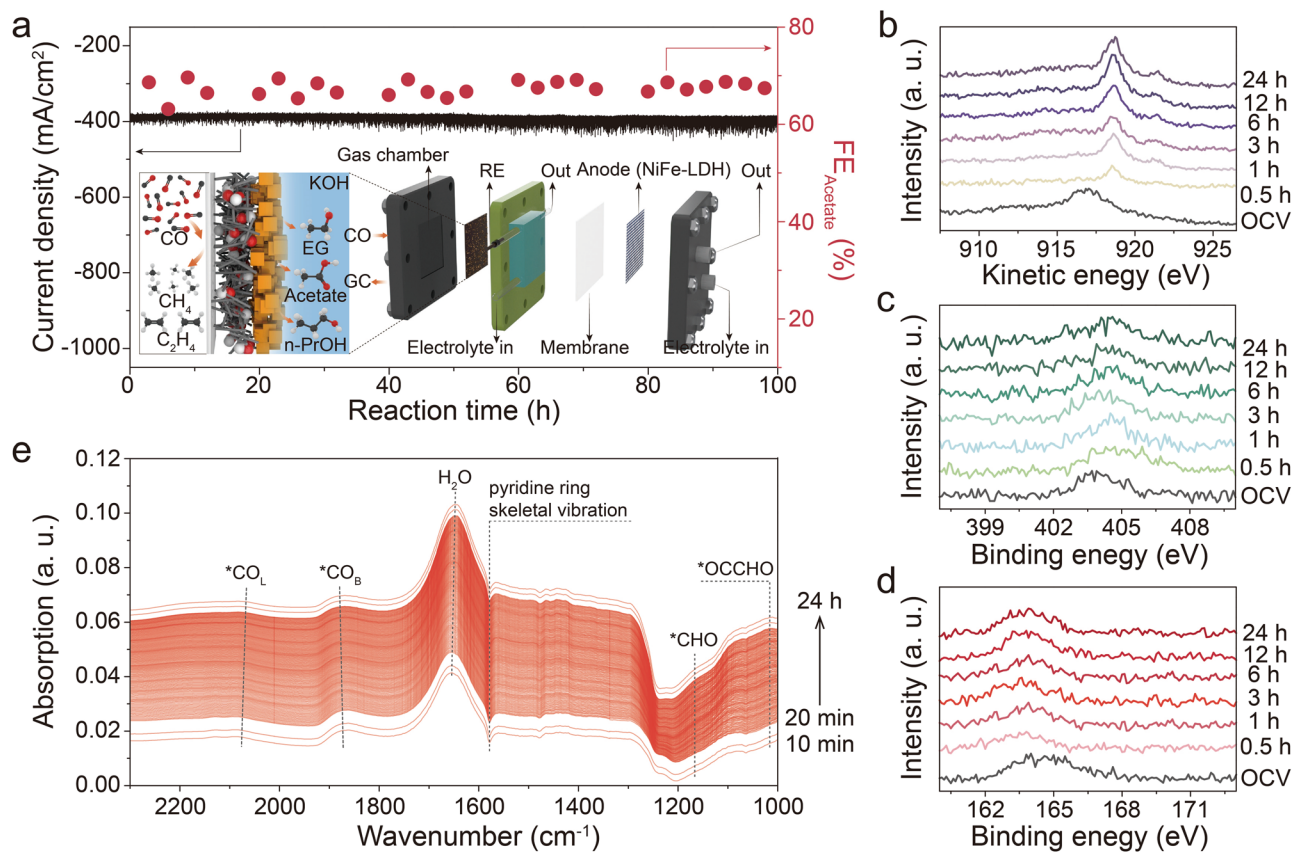


Fig. 2 | Stability evaluation. **a** CORR stability test of $\text{Cu}_2\text{O-pyS}$. Inset is the schematic illustration showing the flow cell. **b** Quasi in-situ time-dependent Cu LMM X-ray-excited Auger electron spectra of $\text{Cu}_2\text{O-pyS}$ collected at -0.65 V vs. RHE . Quasi in-situ time-dependent high-resolution N 1s XPS spectra (c), and S 2p XPS spectra

(d) collected at -0.65 V vs. RHE . **e** In-situ ATR-SEIRAS spectra from 1000 cm^{-1} to 2300 cm^{-1} recorded over $\text{Cu}_2\text{O-pyS}$ in CO-saturated 0.1 mol/L KOH solution at -0.65 V vs. RHE .

hydrogen electrode (RHE). A higher $\text{FE}_{\text{acetate}}$ of 70% could be realized at -0.65 V vs. RHE over $\text{Cu}_2\text{O-pyS}$. As compared to $\text{Cu}_2\text{O-pyS}$, the FE and partial current density towards acetate over unmodified Cu_2O nanocubes are much lower, indicating the critical role of 4-mercaptopyridine played in the CORR (the different electrochemically active surface area (ECSA) contribution could be excluded as shown in Supplementary Fig. 8). To verify the universality of the pyS-modification strategy, commercial Cu, Cu_2O , and CuO were also modified with 4-mercaptopyridine, denoted as c-Cu-pyS, c- $\text{Cu}_2\text{O-pyS}$, and c-CuO-pyS, respectively. After decoration of 4-mercaptopyridine, obvious enhancement in acetate production (selectivity and partial current density) could be observed for all commercial samples (Fig. 1b–d and Supplementary Fig. 9), confirming the generality of the pyS-modification approach. Besides activity and selectivity, stability is also crucial in CORR. The CORR stability of $\text{Cu}_2\text{O-pyS}$ was evaluated in a 9 cm^2 flow cell. As displayed in Fig. 2a, the $\text{Cu}_2\text{O-pyS}$ could be operated continuously at a current density of 380 mA/cm^2 and a $\text{FE}_{\text{acetate}}$ over 60% for 100 h with no noticeable activity decay, outperforming most of the reported state-of-the-art CORR electrocatalysts. It is worth mentioning that 2.08 mol of acetate, derived from superposition of current and Faradaic efficiency, could be produced in 100 h. SEM, TEM, and EDS measurements disclosed that the morphology and size of Cu_2O nanocubes and $\text{Cu}_2\text{O-pyS}$ after CORR were changed (Supplementary Figs. 10 and 11). Both of Cu_2O nanocubes and $\text{Cu}_2\text{O-pyS}$ were reduced to Cu under applied cathodic potentials during CORR (Supplementary Fig. 10a, b). Moreover, N and S could still be observed over $\text{Cu}_2\text{O-pyS}$ after the CORR, indicating that 4-mercaptopyridine was stable under the applied cathodic potential (Supplementary Fig. 11c, d).

Stability evaluation for CORR

To elucidate the structural evolution of $\text{Cu}_2\text{O-pyS}$ during CORR, in-situ Raman spectroscopy was conducted. Raman peaks at 146 and 219 cm^{-1} were observed over Cu_2O nanocubes and $\text{Cu}_2\text{O-pyS}$ at the open circuit potential (OCP) (Supplementary Figs. 12 and 13), which are characteristic Raman peaks of Cu_2O ³⁶. With increase in the applied cathodic potential, the intensity of the Cu_2O characteristic Raman peaks decreased and finally disappeared, suggesting that Cu_2O was reduced to Cu. More importantly, the Raman peaks at 689 and 783 cm^{-1} , which could be assigned to Cu-S vibrational mode, resulting from 4-mercaptopyridine remained stable even at the applied potential of -1.0 V vs. RHE , which is already the CORR working potential for the catalyst, illustrating the excellent affinity of 4-mercaptopyridine over the copper surface. Additionally, Cu-C vibration ($\sim 300\text{ cm}^{-1}$) could also be observed in the in-situ Raman spectra (as shown in Supplementary Fig. 13), resulting from the reactive intermediates in the CORR, which will be discussed later. Quasi in-situ Auger electron spectroscopy (AES) was performed to probe the valance state evolution of Cu during the reaction, where Cu_2O nanocubes was rapidly reduced to Cu^0 after 0.5 h (Fig. 2b). Similar results were also observed in commercial Cu_2O sample (Supplementary Fig. 14). Quasi in-situ time-dependent high-resolution N 1s and S 2p XPS spectra also confirmed that 4-mercaptopyridine could stay on the surface of Cu_2O catalyst at all times (Fig. 2c, d and Supplementary Fig. 15). To further elucidate the structural stability of $\text{Cu}_2\text{O-pyS}$, in-situ time-dependent ATR-SEIRAS measurement was carried out (Supplementary Fig. 16). DFT calculation was performed to identify the positions of the vibrational peaks (Supplementary Fig. 25). Compared to Cu_2O nanocube catalyst, a ATR-SEIRAS peak at around $1,600\text{ cm}^{-1}$ could be observed on $\text{Cu}_2\text{O-pyS}$,

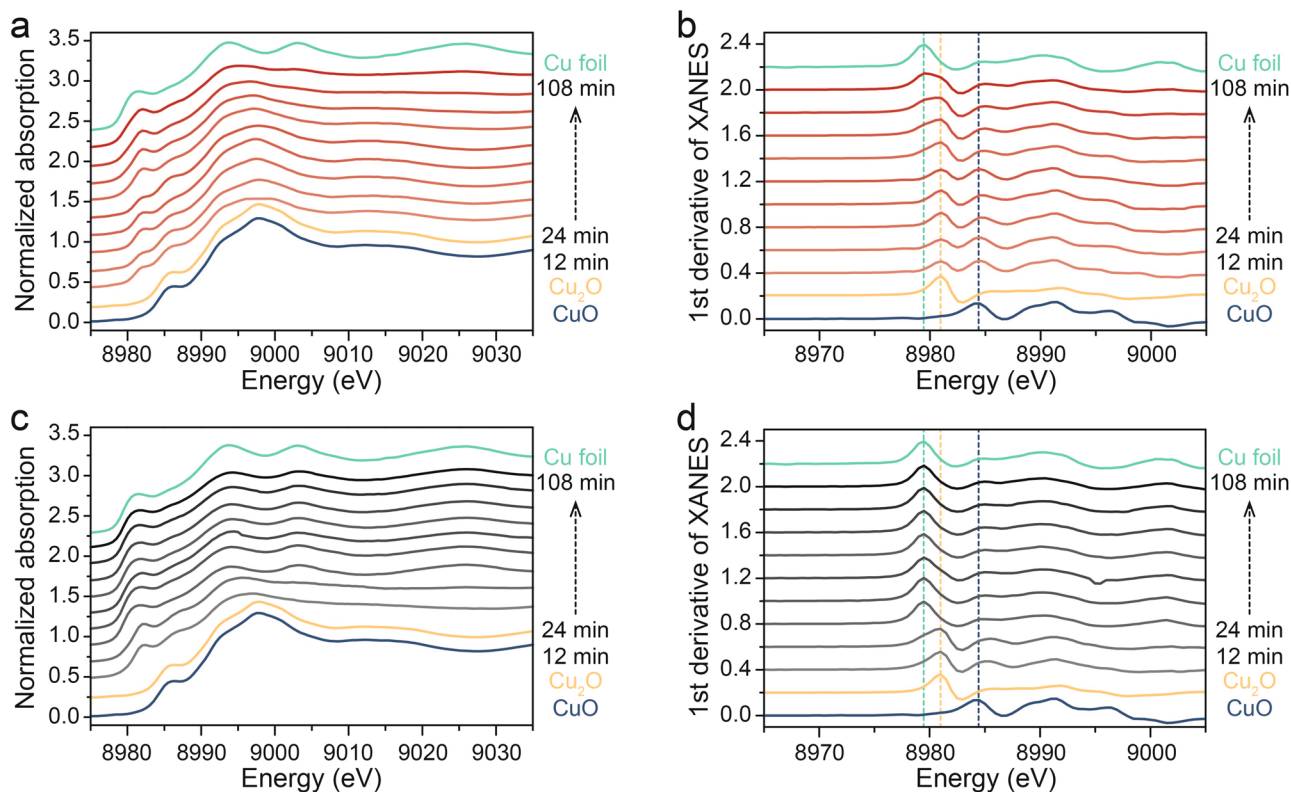


Fig. 3 | In-situ Cu K-edge XANES measurements. **a** In-situ Cu K-edge XANES spectra of Cu_2O nanocubes measured in CO-saturated KOH solution at -0.65 V vs. RHE. **b** The corresponding 1st derivative of XANES at -0.65 V vs. RHE. **c** In-situ Cu

K-edge XANES spectra of Cu_2O -pyS measured in CO-saturated KOH solution at -0.65 V vs. RHE. **d** The corresponding 1st derivative of XANES at -0.65 V vs. RHE.

which can be assigned to pyridine ring skeletal vibration, revealing the successful attachment of 4-mercaptopyridine onto the Cu_2O surface. As shown in Fig. 2e, the pyridine ring skeletal vibration remained in 24 hours of CORR. Moreover, peaks for $^*\text{CO}_L$, $^*\text{CO}_B$, $^*\text{CHO}$, $^*\text{COCHO}$, and H_2O existed throughout the reaction, indicating that 4-mercaptopyridine was stable over the surface of the catalyst (Fig. 2e). X-ray absorption spectroscopy (XAS) was further conducted to disclose the structural and electronic evolution of Cu element. Figure 3a, c revealed that Cu_2O continued to be reduced in CORR. First derivative of X-ray absorption near edge structure (XANES) was analyzed to investigate the reduction of Cu_2O . The results showed that Cu_2O was converted into Cu under the applied cathodic potential, and the transformation was accelerated after decoration of 4-mercaptopyridine (Fig. 3b, d). The k^3 -weighted extended X-ray absorption fine structure (EXAFS) and the corresponding Fourier transform of EXAFS for Cu_2O nanocubes and Cu_2O -pyS recorded during CORR are shown in Supplementary Fig. 17. It is worth mentioning that Cu^0 remained after its appearance, suggesting that Cu_2O (-pyS) derived Cu (-pyS) was the real catalyst for CORR to acetate.

Mechanistic insights for CORR

To further shed light on the underlying role of pyS decoration on CORR, in-situ ATR-SEIRAS measurements under different applied cathodic potentials were performed to probe the reaction intermediates and the reaction pathway. Supplementary Figs. 18 and 19 show the ATR-SEIRAS spectra recorded over Cu_2O nanocubes. Compared to Cu_2O , the water peak at -1625 cm^{-1} is less pronounced on Cu_2O -pyS, suggesting that the presence of pyS can help to reduce water adsorption on the catalyst's surface, which may lower the undesired hydrogen evolution reaction (HER) over Cu_2O . When the applied cathodic potential increased to -0.2 V vs. RHE, several ATR-SEIRAS peaks started to appear over

Cu_2O -pyS. Two types of $^*\text{CO}$ peaks could be found in the ATR-SEIRAS spectra, one at 2080 cm^{-1} , which can be assigned to the linearly bound $^*\text{CO}$ (CO_L); the other at 1800 cm^{-1} , which can be ascribed to the bridge-bound $^*\text{CO}$ (Fig. 4a, b). Both $^*\text{CO}_L$ and $^*\text{CO}_B$ are reactive species in CORR towards acetate formation (Supplementary Figs. 20 and 21). The ratio of $^*\text{CO}_B/^*\text{CO}_L$ over Cu_2O -pyS is much larger than that over Cu_2O , implying that 4-mercaptopyridine could influence $^*\text{CO}$ adsorption configuration (Fig. 4c and Supplementary Figs. 20 and 21). Between the two types of $^*\text{CO}$, $^*\text{CO}_B$ is much easier to participate in the hydrogenation reaction due to its weak C=O bond, in contrast to the strong C≡O bond in $^*\text{CO}_L$ ³⁷. In addition, $^*\text{CHO}$ signal at $1,185$ cm^{-1} and $^*\text{OCCHO}$ signal at $1,040$ cm^{-1} could also be clearly identified over Cu_2O -pyS, which was further supported by the isotope labeling experiments (Supplementary Fig. 22). Previous reports have shown that $^*\text{OCCHO}$ plays as an important intermediate in $\text{CO}_2\text{RR}/\text{CORR}$ to produce acetate³⁸. Figure 4d shows that the ATR-SEIRAS peak ratio of $^*\text{OCCHO}/^*\text{CHO}$ over Cu_2O -pyS is at least one order of magnitude larger than that over Cu_2O , justifying the boosted CORR to acetate over Cu_2O -pyS. The role of $^*\text{OCCHO}$ for CO-to-acetate conversion can be further confirmed by the observation that the $^*\text{OCCHO}$ coverage increased with applied cathodic potential. Two C-C coupling pathways were usually proposed in CORR to produce C_{2+} products (Fig. 4e): the asymmetric $^*\text{CO}$ - $^*\text{CHO}$ coupling for acetate formation and the symmetric $^*\text{CO}$ - $^*\text{CO}$ or $^*\text{CHO}$ - $^*\text{CHO}$ coupling for ethanol and ethylene formation. The detected $^*\text{OCCHO}$ intermediate can only exist in the pathway of asymmetric $^*\text{CO}$ - $^*\text{CHO}$ coupling, explaining the excellent activity and selectivity of CORR to acetate over Cu_2O -pyS. Similar phenomenon could also be observed in the case of commercial Cu_2O and the corresponding c- Cu_2O -pyS, highlighting the importance of 4-mercaptopyridine functionalization (Supplementary Fig. 26). Therefore, 4-mercaptopyridine decoration would be a general strategy

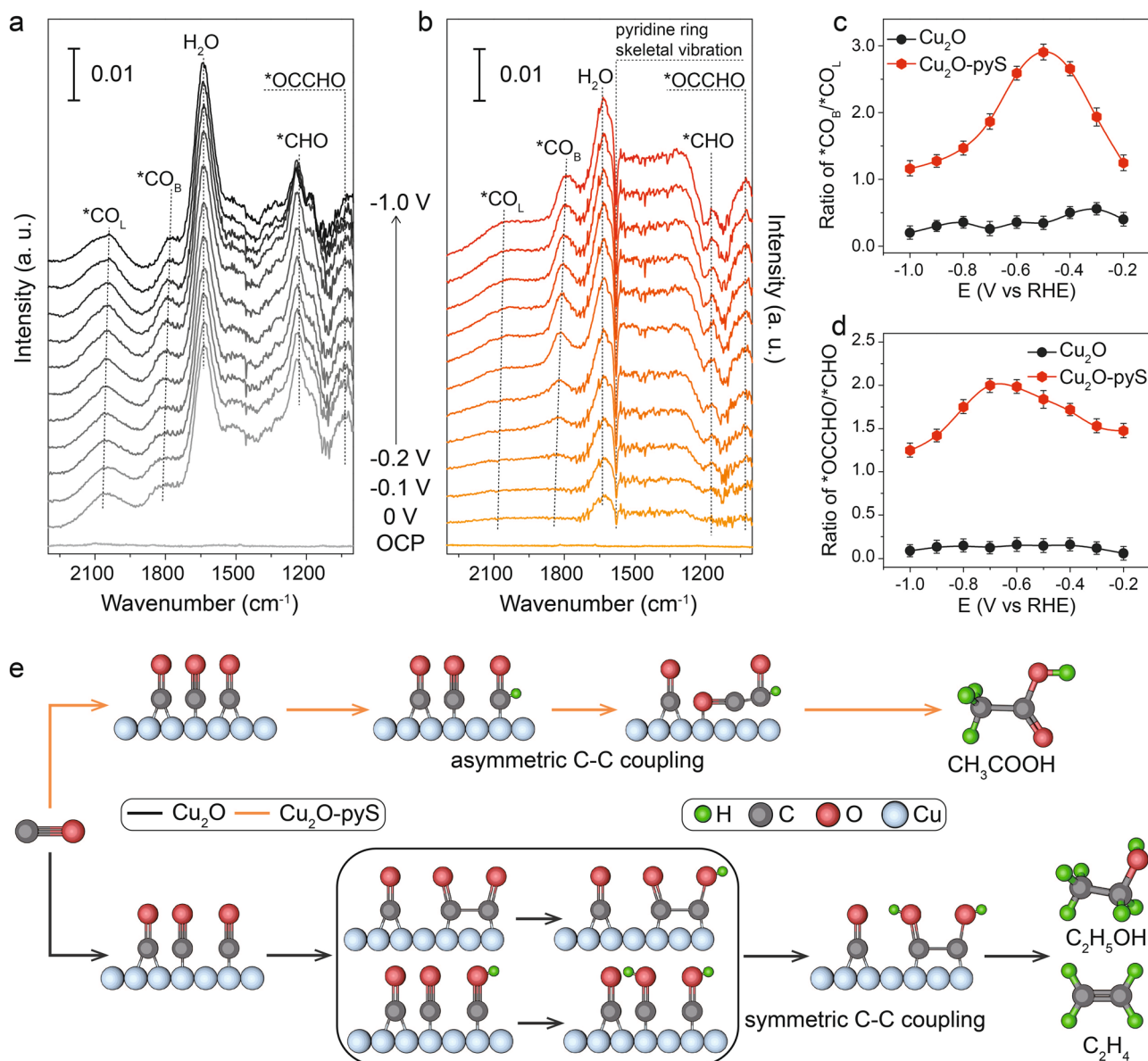


Fig. 4 | In-situ ATR-SEIRAS measurements. In-situ ATR-SEIRAS spectra recorded in a potential window from 0 to -1.0 V vs. RHE over Cu_2O nanocubes (a) and $\text{Cu}_2\text{O-pyS}$ (b) in 0.1 M KOH. c Calculated ratio of $^*\text{CO}_\text{B}/^*\text{CO}_\text{L}$ over Cu_2O nanocubes and $\text{Cu}_2\text{O-pyS}$. d Calculated ratio of $^*\text{OCCHO}/^*\text{CHO}$ over Cu_2O nanocubes and

$\text{Cu}_2\text{O-pyS}$. e Schematic illustration showing the symmetric C-C coupling and asymmetric C-C coupling over Cu_2O nanocubes and $\text{Cu}_2\text{O-pyS}$. Error bars in c and d represent s.d. for each data point ($n = 3$ independent experiments), and points are average values.

to promote CO-to-acetate conversion via boosting asymmetric C-C coupling.

Theoretical understanding

To further investigate the role of 4-mercaptopyridine played in CORR, the 4-mercaptopyridine was intentionally removed from the surface of Cu_2O nanocubes by Ar plasma treatment (the successful removal of 4-mercaptopyridine on Cu_2O nanocubes was confirmed by the disappearance of N and S signals in the XPS spectra as shown in Supplementary Fig. 23b, c). Note that the valence state of Cu decreased slightly after Ar plasma treatment (Supplementary Fig. 23a). Moreover, SEM and TEM images indicate that the morphology and size of Cu_2O nanocubes were maintained after Ar plasma treatment (Supplementary Fig. 23d, e), while the CORR current density and acetate FE were found to decrease sharply after Ar plasma treatment, validating the important role played by 4-mercaptopyridine in CORR to produce

acetate (Supplementary Fig. 23f). On the other hand, thiophenol (pHS) or 2,6-dimethylthiophenol (pyDMS) was also attached onto the surface of Cu_2O nanocubes to explore the contribution of hydrophobicity, C, S or N on CORR (the modified sample is denoted as $\text{Cu}_2\text{O-pHS}$ and $\text{Cu}_2\text{O-pyDMS}$, Supplementary Fig. 24). The acetate FE of CORR over $\text{Cu}_2\text{O-pHS}$ significantly decreased, while that over $\text{Cu}_2\text{O-pyDMS}$ remained nearly unchanged as compared to $\text{Cu}_2\text{O-pyS}$, suggesting that hydrophobicity itself did not play the most significant influence on the performance of CORR and the N atom in 4-mercaptopyridine rather than the S atom governed the CO-to-acetate conversion. To further exclude the contribution of steric effect, a molecule with similar functional group but longer chain (4-(Pyridin-4-yl)thiazole-2-thiol) was used to modify the surface of Cu_2O nanocubes, the performance, as shown in Supplementary Fig. 24, was similar to that of $\text{Cu}_2\text{O-pyS}$ and $\text{Cu}_2\text{O-pyDMS}$, suggesting that the role of steric effect was negligible. To gain a deeper insight into the reaction pathway as

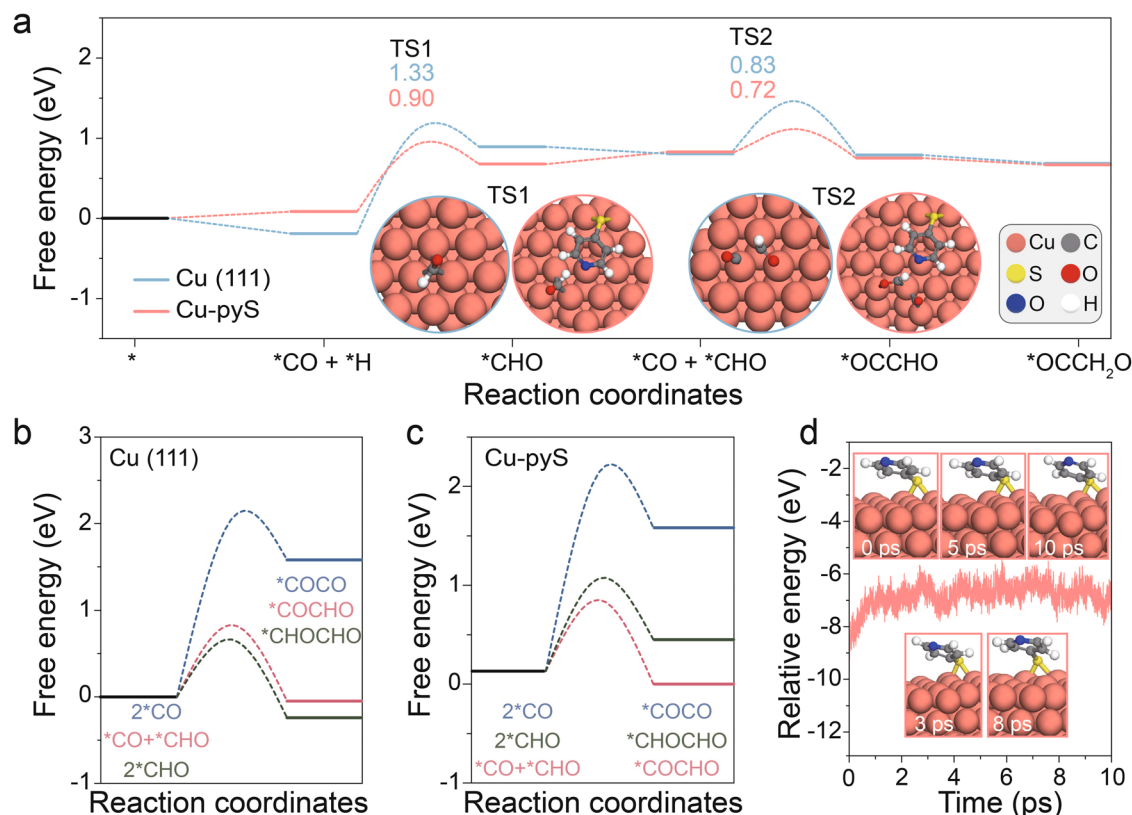


Fig. 5 | DFT calculations. **a** Free energy diagram showing the formation of *CO and *OCCHO . Insets are the models of transitional states over Cu_2O and Cu_2O -pyS. **b** Free energy diagram of symmetric coupling and asymmetric coupling over Cu

(111). **c** Free energy diagram of symmetric coupling and asymmetric coupling over Cu-pyS. **d** Ab initio molecular dynamics (AIMD) results of Cu_2O -pyS. Insets show the side view image of Cu_2O -pyS at 0 ps, 3 ps, 5 ps, 8 ps, and 10 ps.

well as the reaction mechanism, DFT calculations were carried out. Based on ex-situ XRD, in-situ XPS, in-situ Raman spectroscopy and in-situ X-ray absorption spectroscopy (XAS) characterizations, Cu (111) and 4-mercaptopyridine decorated Cu (111) surface were selected as the calculation models to represent Cu_2O nanocubes and Cu_2O -pyS, and the calculated free energy diagrams of CORR are displayed in Supplementary Fig. 27. It is obvious that the energy barrier of CO^*CHO^* asymmetric coupling was much lower than that of CO^*CO^* symmetric coupling over both Cu and Cu-pyS, suggesting that asymmetric coupling was conducive to acetate formation (Fig. 5b, c). Moreover, analyzing coverage of reaction intermediates (including *CO and *CHO) on C-C coupling process ($^*CO + ^*CO$ to *COCO and $^*CO + ^*CHO$ to *COCHO) indicates that the impact of *CHO coverage on ΔG and the corresponding activation barriers is stronger than that of *CO coverage in the $^*CO + ^*CHO$ to *COCHO process (Supplementary Fig. 28). Therefore, *CO hydrogenation to form *CHO is crucial. The rate-determining steps (RDSs) of CORR to form acetate over both Cu_2O and Cu_2O -pyS are *CO hydrogenation and $^*CO^*CHO$ coupling (Fig. 5a). Modifying Cu_2O with 4-mercaptopyridine can decrease the energy barrier of *CO hydrogenation and $^*CO^*CHO$ coupling from 1.33 to 0.9 eV and 1.16 to 0.81 eV, respectively. Note that starting from *CH_2CO , the generation of acetate is exothermic, while the production of ethanol and ethylene are endothermic, revealing the high selectivity towards acetate over Cu-pyS (Supplementary Fig. 27). To explore the origin of the accelerated hydrogenation reaction over Cu_2O -pyS, kinetic isotope effect (KIE) of H/D over Cu_2O nanocubes and Cu_2O -pyS were measured and compared. When H_2O was replaced by D_2O , the formation of acetate reduced obviously over Cu_2O nanocubes with a KIE value of 2.09 and 2.12 at -0.55 V vs. RHE and -0.65 V vs. RHE, respectively, suggesting that the activation and dissociation of water

were included in the RDS of CORR over Cu_2O . On the contrary, the acetate formation using D_2O remained nearly undisturbed over Cu_2O -pyS with a KIE value of 1.13 and 1.11 at -0.55 V vs. RHE and -0.65 V vs. RHE, respectively. The value approached 1, suggesting that the dissociation of water was not included in the RDS of CORR over Cu_2O -pyS and therefore the hydrogenation of *CO could be expedited over Cu_2O -pyS (Supplementary Fig. 29). DFT calculation disclosed that hydrogenation of *CO_B was more energetically favorable than that of *CO_L , confirming that hydrogenation steps were accelerated over Cu_2O -pyS (Supplementary Fig. 31). Moreover, water dissociation was found to be propelled after the introduction of 4-mercaptopyridine (Supplementary Fig. 32a). N atom in 4-mercaptopyridine assisted to capture one H atom from water, facilitating water dissociation and the subsequent hydrogenation process (Supplementary Fig. 32b). Supplementary Fig. 30 shows charge redistribution occurred between the N atom in 4-mercaptopyridine and the H atom in *CHO and *OCCHO , indicating that 4-mercaptopyridine was beneficial to stabilize *CHO and *OCCHO . Supplementary Fig. 30 presents the differential charge density for various important CORR intermediates over Cu_2O and Cu_2O -pyS. $^*CO + ^*H$ was found more stable over Cu_2O , while *CHO and *OCCHO were more stable over Cu_2O -pyS. These observations suggest the role of hydrogen bond in stabilizing *CHO and *OCCHO , which can help to break the Brønsted-Evans-Polanyi (BEP) scaling relationship and boost CO-to-acetate conversion. The projected density of states (PDOS) analysis was then performed to get a better understanding of the reaction mechanism. For $^*CO + ^*H$ step, the Cu d-orbital of Cu_2O -pyS exhibits more overlapping with the H s-orbital, indicating favorable hydrogenation of *CO and undesirable HER over Cu_2O -pyS (Supplementary Fig. 33a, b). For *CHO , more overlapping between the Cu d-orbital of Cu_2O -pyS and the C p-orbital of *CHO was observed and

at the same time the N p-orbital of Cu₂O-pyS overlapped with the H s-orbital of *CHO, corroborating that *CHO was more stable over Cu₂O-pyS (Supplementary Fig. 33c, d). For *OCCHO, enhanced overlapping between the Cu d-orbital of Cu₂O-pyS and the C/O p-orbital of *CHO as well as the N p-orbital of Cu₂O-pyS and the H s-orbital of *CHO were noticed, justifying the stabilization effect of 4-mercaptopyridine on *OCCHO (Supplementary Fig. 33e, f). The enhanced adsorption to CORR intermediates over Cu₂O-pyS can be also supported by its higher d-band center (Supplementary Fig. 34). Based on the above investigations, the reaction pathways of CORR towards various products over Cu₂O and Cu₂O-pyS are proposed as shown in Supplementary Figs. 35 and 36. To further examine the stability of Cu₂O-pyS, Ab initio molecular dynamics (AIMD) simulation was performed. No noticeable geometry change could be observed throughout the AIMD simulation, verifying the thermodynamic and kinetic durability of Cu₂O-pyS, matching well with the experiments (Fig. 5d).

Discussion

To sum up, we have developed a general solution method to prepare 4-mercaptopyridine modified Cu-based catalysts, including commercial Cu, Cu₂O, CuO and the synthesized Cu₂O nanocubes, which exhibit excellent electrochemical CORR performance to produce acetate. The total current density can reach approximately 380 mA/cm² with an acetate FE beyond 60% in a flow cell. In-situ ATR-SEIRAS observes stronger *CO signal with bridge configuration and stronger *OCCHO signal over Cu₂O-pyS than unmodified Cu₂O during CORR. DFT calculations illustrate that local molecular modification can effectively tune the electronic structure of copper catalyst and strengthen *CO and *CHO intermediates adsorption by the stabilization effect through hydrogen bonding, which greatly promotes the asymmetric *CO-*CHO coupling in electrochemical CORR, resulting in an exceptional CO-to-acetate conversion performance.

Methods

Chemicals and materials

Copper (II) chloride (CuCl₂), sodium hydroxide (NaOH), ascorbic acid (C₆H₈O₆), 4-mercaptopyridine (C₅H₅NS), thiophenol (C₆H₅SH), 2,6-dimethylbenzenethiol (C₈H₁₀S) and isopropanol (C₃H₈O) were purchased from Sigma-Aldrich. All chemicals were used directly without further purification. De-ionized water (DI water) was obtained from Millipore Q water purification system.

Synthesis of Cu₂O nanocubes

Cu₂O nanocubes were synthesized by an ascorbic acid reduction method at room temperature. Typically, 0.1 mmol of CuCl₂ was dissolved in 40 mL of DI water, followed by dropwisely adding 2.5 mL of NaOH aqueous solution (0.2 mol/L). Then the solution was stirred for 5 minutes, followed by dropwisely adding 2.5 mL of ascorbic acid solution (1 mol/L). The mixture was further stirred for another 5 minutes. Finally, the product was harvested by centrifugation and then washed with ethanol thoroughly.

Synthesis of Cu₂O-pyS

The as-prepared Cu₂O nanocubes were dispersed in N, N-dimethylformamide (DMF) and sonicated for 30 minutes at room temperature, followed by adding a solution containing 4-mercaptopyridine under inert atmosphere. Subsequently, the suspension was sonicated for another 3 hours. Finally, the product was harvested by centrifuge and then washed with DMF and ethanol thoroughly.

Synthesis of c-Cu (Cu₂O/CuO)-pyS

The commercial Cu powder (25 nm, Sigma), Cu₂O powder and CuO powder were dispersed in N, N-dimethylformamide (DMF) and sonicated for 30 minutes at room temperature, followed by adding a

solution containing 4-mercaptopyridine under inert atmosphere. Subsequently, the suspension was sonicated for another 3 hours. Finally, the product was harvested by centrifuge and then washed with DMF and ethanol thoroughly.

Materials characterization

Powder XRD was performed on a Bruker D2 Phaser using Cu K α radiation with a LYNXEYE detector at 30 kV and 10 mA. The morphological information was examined with field-emission SEM (FESEM, JEOL JSM-6700F). Sub angstrom-resolution high-angle annular dark field scanning transmission electron microscopy (HAADFSTEM) characterization was conducted on a JEOL JEMARM200F STEM with a guaranteed resolution of 0.08 nm. Raman spectra were recorded on a Renishaw INVIA Reflex Raman spectrometer using 514 nm laser as the excitation source. XPS measurements were carried out on a Thermo-fisher ESCALAB 250Xi photoelectron spectrometer (ThermoFisher Scientific) using a monochromatic Al K α X-ray beam (1,486.6 eV)³⁹.

Electrode fabrication

A catalyst ink solution containing 10 mg of Cu₂O-pyS, 0.98 mL of DI water, 0.98 mL of isopropanol and 40 μ L of Nafion ionomer solution (5 wt.% in H₂O) was mixed and sonicated for at least 3 hours. Then, the ink was deposited onto a carbon paper to achieve a catalyst loading of ~1 mg/cm². Cu₂O electrode was also prepared using the same method. To ensure precise control of the catalytic layer thickness and achieve good uniformity, we employed ultrasonic spraying method to prepare the electrode. This involves two steps: (1) Ultrasonic dispersion to prepare catalyst paste; (2) Atomization and ultrasonic spraying of the catalyst slurry onto a support body, which can be either a gas diffusion layer or proton exchange membrane.

Electrochemical measurements

CORR was performed in 1 M KOH solution in a three-channel flow cell. The anode and the cathode were separated by a hydroxide exchange membrane. Hg/HgO electrode was used as the reference electrode, while NiFeMoB developed by our research group⁴⁰ was deployed as the anode catalyst. The gas flow rate was 20 sccm. The products of CORR were quantified using a gas chromatography (Agilent 7890) equipped with a flame ionization detector (FID) and a thermal conductivity detector (TCD) and a high-performance liquid chromatography (Agilent Technologies 1260 Infinity) equipped with a RID detector. Acetate measurements were conducted only in the cathode chamber.

In-situ ATR-SEIRAS measurements

The attenuated total reflectance surface enhanced infrared absorption spectroscopy (ATR-SEIRAS) measurements were performed on a Nicolet iS50 FTIR spectrometer equipped with a MCT detector cooled with liquid nitrogen and PIKE VeeMAX III variable angle ATR sampling accessory.

Quasi in-situ XPS measurements

The X-ray photoelectron spectroscopy (XPS) measurements were performed on a SPECS NAP-XPS interconnected with a glovebox (Vigor Corp) (Supplementary Fig. 15). The CORR were performed in the glovebox, afterwards the sample was transferred to the XPS chamber without air exposure.

In-situ Raman measurements

In-situ Raman spectroscopy measurements were conducted in a custom-designed three-electrode SERS flow cell with a saturated Ag/AgCl electrode as the reference electrode and a graphite rod as the counter electrode in the anode chamber. During the measurements, the electrolyte was constantly purged with CO gas and circulated across the cell using a peristaltic pump. The Raman measurements were performed on a LabRAM HR Evolution microscope (Horiba Jobin

Yvon) with a 532 nm laser, a 50× objective, a monochromator (600 grooves/mm grating), and a CCD detector⁴¹.

Computational methods

All spin-polarized DFT geometry optimizations were implemented under the description of generalized gradient approximation (GGA) based PBE-D3 functional with VASPsol model in the Vienna ab initio Simulation Package (VASP5.4.4). The 4 × 4 periodic rectangular supercell Cu (111) was built to support the 4-mercaptopyridine. The Brillouin zone was sampled by 3 × 3 × 1 Monkhorst-Pack k-point scheme, and the cutoff was set as 450 eV. The convergence criteria were set as 10⁻⁵ eV in energy and 0.01 eV Å⁻¹ in force, respectively. A 20 Å vacuum space was added along the perpendicular direction to eliminate the effects of periodic images. The climbing image nudged elastic band (CI-NEB) method was employed with converged forces less than 0.05 eV/Å in VTST package to obtain transition states to derive the reaction free energy barriers⁴². During structure relaxation, the bottom two layers of copper atoms were immobilized, while all other ions were allowed to move freely to reasonably save computing resources. The canonical ensemble (NPT) ab initio molecular dynamic (AIMD) simulations were carried out in the Andersen thermostat at 298 K for 10 picoseconds (ps) with a time step of 1 femtosecond (fs).

In each of the electroreduction elementary steps, the reaction Gibbs free energy (ΔG) was calculated with consideration of thermal internal energy contribution according to:

$$\Delta G = \Delta E + \Delta E_{ZPE} - T\Delta S + G_U + G_{pH}$$

where ΔE , ΔE_{ZPE} and $T\Delta S$ are the changes of electronic energy, the zero-point energy, and the temperature-entropy product in each elementary step. ΔG_U and ΔG_{pH} equaling to $-eU$ and $k_B T \ln 10 \times \text{pH}$ (here $\text{pH} = 14$) are the contribution of applied electrode potential and pH to ΔG . The entropy of $\text{H}^+ + \text{e}^-$ pair is approximately half of H_2 entropy in standard condition.

Data availability

All data are reported in the main text and supplementary materials. Source data are provided with this paper. All relevant data are available from the authors on reasonable request. Source data are provided with this paper.

References

- Flexer, V. & Jourdin, L. Purposely designed hierarchical porous electrodes for high rate microbial electrosynthesis of acetate from carbon dioxide. *Acc. Chem. Res.* **53**, 311–321 (2020).
- Ji, Y. et al. Selective CO-to-acetate electroreduction via intermediate adsorption tuning on ordered Cu–Pd sites. *Nat. Catal.* **5**, 251–258 (2022).
- Matias, I. A., Ribeiro, A. P. & Martins, L. M. Selective oxidation of ethane to acetic acid catalyzed by a C-scorpionate iron (II) complex: a homogeneous vs. heterogeneous comparison. *Molecules* **25**, 5642 (2020).
- Kalck, P., Le Berre, C. & Serp, P. Recent advances in the methanol carbonylation reaction into acetic acid. *Coord. Chem. Rev.* **402**, 213078 (2020).
- Thomas, C. M. & Süß-Fink, G. Ligand effects in the rhodium-catalyzed carbonylation of methanol. *Coord. Chem. Rev.* **243**, 125–142 (2003).
- Forster, D. On the mechanism of a rhodium-complex-catalyzed carbonylation of methanol to acetic acid. *J. Am. Chem. Soc.* **98**, 846–848 (1976).
- Ni, Y. et al. A green route for methanol carbonylation. *Catal. Sci. Technol.* **7**, 4818–4822 (2017).
- Zhang, J., Cai, W., Hu, F. X., Yang, H. & Liu, B. Recent advances in single atom catalysts for the electrochemical carbon dioxide reduction reaction. *Chem. Sci.* **12**, 6800–6819 (2021).
- Boutin, E. et al. Aqueous electrochemical reduction of carbon dioxide and carbon monoxide into methanol with cobalt phthalocyanine. *Angew. Chem. Int. Ed.* **58**, 16172–16176 (2019).
- Rabiee, H. et al. Gas diffusion electrodes (GDEs) for electrochemical reduction of carbon dioxide, carbon monoxide, and dinitrogen to value-added products: a review. *Energy Environ. Sci.* **14**, 1959–2008 (2021).
- Hori, Y., Murata, A., Kikuchi, K. & Suzuki S. Electrochemical reduction of carbon dioxides to carbon monoxide at a gold electrode in aqueous potassium hydrogen carbonate. *J. Chem. Soc. Chem. Commun.* **10**, 728–729 (1987).
- Liu, X. et al. Understanding trends in electrochemical carbon dioxide reduction rates. *Nat. Commun.* **8**, 1–7 (2017).
- Gu, Z. et al. Efficient electrocatalytic CO₂ reduction to C₂₊ alcohols at defect-site-rich Cu surface. *Joule* **5**, 429–440 (2021).
- Zhong, D. et al. Coupling of Cu (100) and (110) facets promotes carbon dioxide conversion to hydrocarbons and alcohols. *Angew. Chem. Int. Ed.* **60**, 4879–4885 (2021).
- Kim, Y. et al. Time-resolved observation of C–C coupling intermediates on Cu electrodes for selective electrochemical CO₂ reduction. *Energy Environ. Sci.* **13**, 4301–4311 (2020).
- Morales-Guio, C. G. et al. Improved CO₂ reduction activity towards C₂₊ alcohols on a tandem gold on copper electrocatalyst. *Nat. Catal.* **1**, 764–771 (2018).
- Chang, X. et al. C–C coupling is unlikely to be the rate-determining step in the formation of C₂₊ products in the copper-catalyzed electrochemical reduction of CO. *Angew. Chem.* **134**, e202111167 (2022).
- Duan, G. Y. et al. Highly efficient electrocatalytic CO₂ reduction to C₂₊ products on a poly (ionic liquid)-based CuO–CuI tandem catalyst. *Angew. Chem. Int. Ed.* **61**, e202110657 (2022).
- Yang, J. et al. Residual chlorine induced cationic active species on porous Cu electrocatalyst for highly stable electrochemical CO₂ reduction to C₂₊. *Angew. Chem.* **60**, 11487–11493 (2021).
- Gao, D. et al. Selective CO₂ electroreduction to ethylene and multicarbon alcohols via electrolyte-driven nanostructuring. *Angew. Chem.* **131**, 17203–17209 (2019).
- Wang, Y. et al. Catalyst synthesis under CO₂ electroreduction favours faceting and promotes renewable fuels electrosynthesis. *Nat. Catal.* **3**, 98–106 (2020).
- Li, Y. et al. Electrochemically scrambled nanocrystals are catalytically active for CO₂-to-multicarbon. *Proc. Natl. Acad. Sci. USA* **117**, 9194–9201 (2020).
- Zhang, G. et al. Efficient CO₂ electroreduction on facet-selective copper films with high conversion rate. *Nat. Commun.* **12**, 1–11 (2021).
- Xie, M. S. et al. Amino acid modified copper electrodes for the enhanced selective electroreduction of carbon dioxide towards hydrocarbons. *Energy Environ. Sci.* **9**, 1687–1695 (2016).
- Creissen, C. E. et al. Molecular inhibition for selective CO₂ conversion. *Angew. Chem. Int. Ed.* **61**, e202206279 (2022).
- Pankhurst, J. R., Iyengar, P., Louidice, A., Mensi, M. & Buonsanti, R. Metal–ligand bond strength determines the fate of organic ligands on the catalyst surface during the electrochemical CO₂ reduction reaction. *Chem. Sci.* **11**, 9296–9302 (2020).
- Li, F. W. et al. Molecular tuning of CO₂-to-ethylene conversion. *Nature* **23**, 509–513 (2020).
- Tamura, J. et al. Electrochemical reduction of CO₂ to ethylene glycol on imidazolium ion-terminated self-assembly monolayer-modified Au electrodes in an aqueous solution. *Phys. Chem. Chem. Phys.* **17**, 26072–26078 (2015).

29. Fang, Y. & Flake, J. C. Electrochemical reduction of CO₂ at functionalized Au electrodes. *J. Am. Chem. Soc.* **139**, 3399–3405 (2017).
 30. Luo, M. C. et al. Coordination polymer electrocatalysts enable efficient CO-to-acetate conversion. *Adv. Mater.* **35**, 2209567 (2023).
 31. Herrera, S. et al. Surface structure of 4-mercaptopyridine on Au (111): a new dense phase. *Langmuir* **33**, 9565–9572 (2017).
 32. Yang, H. B. et al. Atomically dispersed Ni (i) as the active site for electrochemical CO₂ reduction. *Nat. Energy* **3**, 140–147 (2018).
 33. Weekes, D. M., Salvatore, D. A., Reyes, A., Huang, A. & Berlinguette, C. P. Electrolytic CO₂ reduction in a flow cell. *Acc. Chem. Res.* **51**, 910–918 (2018).
 34. Nguyen, T. N. & Dinh, C.-T. Gas diffusion electrode design for electrochemical carbon dioxide reduction. *Chem. Soc. Rev.* **49**, 7488–7504 (2020).
 35. Feng, Y. et al. Te-doped Pd nanocrystal for electrochemical urea production by efficiently coupling carbon dioxide reduction with nitrite reduction. *Nano Lett* **20**, 8282–8289 (2020).
 36. Deng, S. et al. Reduced graphene oxide conjugated Cu₂O nanowire mesocrystals for high-performance NO₂ gas sensor. *J. Am. Chem. Soc.* **134**, 4905–4917 (2012).
 37. Bai, H. et al. Controllable CO adsorption determines ethylene and methane productions from CO₂ electroreduction. *Sci. Bull.* **66**, 62–68 (2021).
 38. Bertheussen, E. et al. Acetaldehyde as an intermediate in the electroreduction of carbon monoxide to ethanol on oxide-derived copper. *Angew. Chem.* **128**, 1472–1476 (2016).
 39. Gao, J. J. et al. Enabling direct H₂O₂ production in acidic media through rational design of transition metal single atom catalyst. *Chem* **3**, 658–674 (2020).
 40. Cai, W. Z. et al. Amorphous multimetal alloy oxygen evolving catalysts. *ACS Mater. Lett.* **2**, 624–632 (2020).
 41. He, M. et al. Selective enhancement of methane formation in electrochemical CO₂ reduction enabled by a Raman-inactive oxygen-containing species on Cu. *ACS Catal* **12**, 6036–6046 (2022).
 42. Li, F. H., Wen, H. Q. & Tang, Q. Reaction mechanism and kinetics for carbon dioxide reduction on iron–nickel Bi-atom catalysts. *J. Mater. Chem. A* **10**, 13266–13277 (2022).
- Science Foundation of China (No. 22208021, 21974103, 22102207, 2199152, and 21832004) and Photon Science Research center for Carbon Dioxide.

Author contributions

J.D. and F.L. contributed equally. J.D., F.L., H.Y., T.Z. and B.L. conceived the project. B.L. supervised the project. J.D., X.R., Yu.L., Yi.L., Z.S., T.W., W.W., Y.W. and Y.C. performed the experimental study. T.Z., F.L. and Y.W. performed the theoretical study. J.D., F.L. H.Y., T.Z. and B.L. wrote the manuscript with support from all authors.

Competing interests

The authors declare no competing interests.

Additional information

Supplementary information The online version contains supplementary material available at <https://doi.org/10.1038/s41467-024-47913-1>.

Correspondence and requests for materials should be addressed to Hongbin Yang, Tianyu Zhang or Bin Liu.

Peer review information *Nature Communications* thanks Cao-Thang Dinh and the other, anonymous, reviewers for their contribution to the peer review of this work. A peer review file is available.

Reprints and permissions information is available at <http://www.nature.com/reprints>

Publisher's note Springer Nature remains neutral with regard to jurisdictional claims in published maps and institutional affiliations.

Open Access This article is licensed under a Creative Commons Attribution 4.0 International License, which permits use, sharing, adaptation, distribution and reproduction in any medium or format, as long as you give appropriate credit to the original author(s) and the source, provide a link to the Creative Commons licence, and indicate if changes were made. The images or other third party material in this article are included in the article's Creative Commons licence, unless indicated otherwise in a credit line to the material. If material is not included in the article's Creative Commons licence and your intended use is not permitted by statutory regulation or exceeds the permitted use, you will need to obtain permission directly from the copyright holder. To view a copy of this licence, visit <http://creativecommons.org/licenses/by/4.0/>.

© The Author(s) 2024

Acknowledgements

We acknowledge funding support from the City University of Kong Hong startup fund (9020003), ITF-RTH - Global STEM Professorship (9446006), the National Key Research and Development Program of China (No. 2022YFA1506200), CAS Project for Young Scientists in Basic Research (YSBR-022), the Strategic Priority Research Program of the Chinese Academy of Sciences (XDB36030200), the National Natural Science Foundation of China (Grant No. 22075195), the National Natural